ACS APPLIED MATERIALS & INTERFACES

Research Article

Cite This: ACS Appl. Mater. Interfaces 2018, 10, 28159−28165

www.acsami.org

Origin of Hydrophilic Surface Functionalization-Induced Thermal Conductance Enhancement across Solid−Water Interfaces

Dezhao Huang,[†] Ruimin Ma,[†] Teng Zhang,[†,§] and Tengfei Luo*[,†,‡]

[†]Department of Aerospace and Mechanical Engineering, University of Notre Dame, Notre Dame, Indiana 46556, United States

[‡]Chemical and Biomolecular Engineering, University of Notre Dame, Notre Dame, Indiana 46556, United States

ABSTRACT: Thermal transport across solid−water interfaces is critical for a wide range of applications such as solar thermal evaporation, nanoparticle-assisted hyperthermia therapeutics, and nanofluids. Surface functionalization using self-assembled monolayers (SAMs) to change the hydrophilicity of the solid surface is a common strategy to improve the thermal conductance of solid−water interfaces. Although it is known that hydrophilic interfaces increase the interfacial bonding, how it impacts the molecular level energy transport across the interface is still not clear. In this paper, we perform molecular dynamics simulations to calculate the thermal conductance of differently functionalized gold (Au)−water interfaces. Combining the heat flux decomposition to different interatomic interactions across interfaces and analyses of water structures close to the functionalized surfaces, we found that there is a collaborative effect from the electrostatic interactions and the Lennard-Jones (L-J) interactions (especially the repulsive part). The electrostatic interactions, which are between the polar functional groups of SAMs and water, will attract water molecules closer to the SAM surface, leading both the electrostatic and L-J interactions to have larger effective forces across the interfaces. This increases the power exchanged between solid and water atoms, enhancing the thermal energy transport. The results from this work will provide new insights to the understanding of thermal transport across solid−water interfaces.

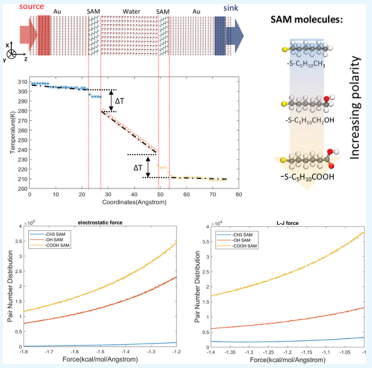

KEYWORDS: *hard−soft interface, self-assembled monolayer, interfacial thermal conductance, nonequilibrium molecular dynamics, interfacial heat flux*

INTRODUCTION

Thermal transport across solid−water interfaces is critical for a wide range of applications from solar thermal water treatment[1−4] and nanofluids[5−7] to nanoparticle-assisted photothermal therapeutics.[1,8−12] The interfacial thermal resistance can play important or even dominant roles in heat transfer when the system's constituent length reaches the nanometer scale.[13−17] Surface functionalization using self-assembled monolayers (SAMs)[18] to change the interfacial adhesion energy between the hard and soft interface is a common strategy to improve the interfacial thermal conductance (ITC) and it has been studied both computationally and experimentally.[19−21] Research has found positive relationships between the interfacial adhesion energy and ITC across the solid−water interfaces experimentally.[22,23] Similar conclusions have also been obtained from a number of molecular dynamics (MD) simulations.[24−31] Although it is generally known that stronger interfacial adhesion energy can enhance the ITC, how it impacts the molecular level energy transport mechanism across the interface is still not clear. Because interfacial thermal transport is related to the dynamics of atomic motion and interatomic forces between the atoms at each side of the interface,[32] the interfacial adhesion energy, which is a static property, cannot be directly linked to the thermal conductance.

In this study, we use nonequilibrium MDs (NEMD) simulations to study the thermal transport across gold (Au)−water interfaces with the Au surfaces functionalized by different SAMs. Three different SAMs are studied to systematically change the surface hydrophobicity. A positive relation between the interfacial binding energy and the ITC is observed. To understand the underlying mechanism, we characterize the interfacial heat flux via the atomic velocity and interfacial forces. We also decompose the interfacial interaction and thermal transport into contributions from Lennard-Jones (L-J) and electrostatic forces and relate their impacts on the interatomic distances between the SAM head groups and water molecules to ITC. It is found that there is a collaborative effect from the electrostatic interaction and the repulsive part of the L-J interaction. The electrostatic interactions, which are between the highly polarized functional groups of SAMs and water, will attract water molecules closer to the solid surface, leading both electrostatic and repulsive interactions to have larger effective forces across the interface, which in turn result in larger ITC. These results may provide new insights to the understanding of the mechanism of thermal transport across solid−water interfaces.

Received: March 5, 2018
Accepted: July 30, 2018
Published: July 30, 2018

DOI: 10.1021/acsami.8b03709
ACS Appl. Mater. Interfaces 2018, 10, 28159−28165

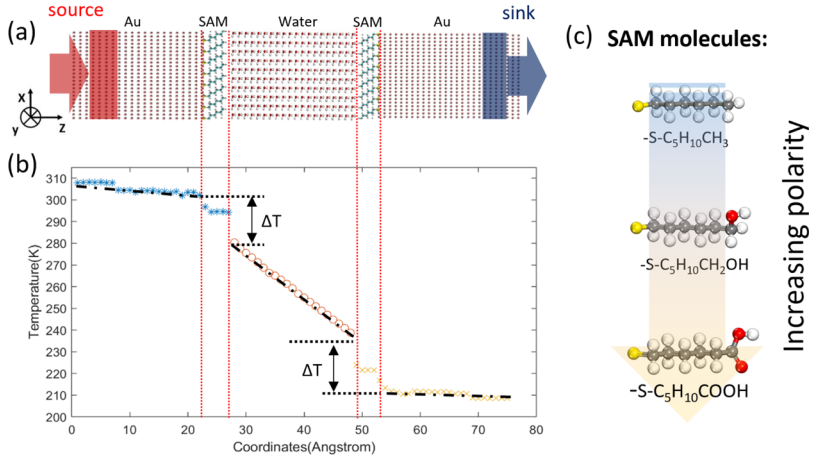

Figure 1. (a) Simulation system setup for ITC calculations via NEMD: heat flows from source to sink across the junction. (b) Temperature profile across the simulation domain and the definition of the interfacial temperature difference. (c) Molecular structures of the SAM molecules studied. From top to bottom, the functional groups of these molecules become more polarized.

SIMULATION METHODS

In this study, the model consisted of three types of thiol SAM molecules chemically adsorbed on the Au(111) surface with explicitly defined TIP3P model water molecules. Three different terminal groups were studied including 1-hexanethiol (HS−$(CH_2)_5$−CH_3), 6-mercapto-1-hexanol (HS−$(CH_2)_6$−OH), and 6-mercaptohexanoic acid (HS−$(CH_2)_5$−COOH). For brevity, they are denoted as −CH_3 SAM, −OH SAM, and −COOH SAM, respectively (Figure 1). These three types of SAM molecules feature functionalizations with a range of hydrophilicities. The expected hydrophilicity with respect to water increases from the −CH_3 SAM to the −OH SAM and then to the −COOH SAM, as the head groups become more polarized. Specifically, the −COOH SAM has an epoxy and a hydroxyl group, which can both form hydrogen bonds with neighboring water molecules and thus should provide the highest interface energy among these three types of SAMs. This trend has been experimentally observed through the hysteresis contact angle experiment from Harikrishna et al.[22] We should mention that the backbone and length effect have been considered in the previous Zhang's work.[33] In this way, we can largely isolate the effect of surface hydrophilicity on the ITC for these three types of surface functionalizations.

In the MD simulations, the Morse potential is

$$E(r) = D_0[e^{-2\alpha(r-r_0)} - 2e^{-\alpha(r-r_0)}] \quad (1)$$

where D_0 is the bond-dissociation energy, r_0 is the equilibrium bond length, and α is the parameter characteristic of the atom, which is used to simulate the gold atoms and the bond interaction between the Au substrate and the sulfur (S) atoms in the thiol SAM molecules. Such a potential has been previously used for SAM-on-Au structures successfully.[34−36] The water molecules are modeled using the TIP3P model,[37] which reproduces water thermodynamic and structural properties well.[38] The polymer consistent force field is adopted to simulate the SAM molecules,[39] which has been successfully used for thermal transport studies involving SAMs.[33,40] The nonbonded interactions between Au and other atoms are simulated by the L-J interaction

$$E = 4\varepsilon\left[\left(\frac{\sigma}{r_{ij}}\right)^{12} - \left(\frac{\sigma}{r_{ij}}\right)^{6}\right] \quad (2)$$

where ε and σ are the representative scales of energy and length and r_{ij} is the distance between two molecules, i and j. L-J interaction parameters are chosen from a modified universal force field,[41,42] except for the S atoms which are bound covalently to Au. All pair coefficients associated with Au atoms are listed in Table 1. A cutoff of 8 Å is used for the Morse potential, and 10 Å is chosen for the L-J interactions. The long-range electrostatic interaction in the entire system is computed by the particle−particle particle−mesh approach with an accuracy of 1×10^{-5}. Simulations are performed using the large-scale atomic/molecular massively parallel simulator.[43] A time step size of 0.25 fs is chosen because of the presence of lightweighted hydrogen atoms.[34,35,44]

Table 1. Morse Potential D_0, r_0, α Parameters for Interactions within Au and between Au and S Atoms[a]

pair type	D_0, kcal/mol	α, 1/Å	r_0, Å
Au−Au	10.954	1.583	3.042
Au−S	8.763	1.47	2.65
pair type	ε, kcal/mol		σ, Å
Au−C_3	0.0634		3.182
Au−C_2	0.0634		3.182
Au−H_c	0.0414		2.752
Au−H_o	0.0414		2.752
Au−O_2	0.0484		3.026
Au−O_1	0.0484		3.026
Au−O_w	0.141		3.6

[a]L-J potential ε and σ parameters between Au atoms and the rest atoms. "C_3" represents the carbon atom in the methyl group of the −CH_3 SAM, and "C_2" represents the carbon atom in the backbone of SAMs. "H_c" represents the hydrogen atom connected to carbon atoms. "H_o" represents the hydrogen atom in the hydroxyl and carboxyl groups in the −OH and −COOH SAMs. "O_1" represents the oxygen atoms in the hydroxyl groups in the −OH and −COOH SAMs. "O_2" is the double-bond oxygen atom in the carboxyl group in the −COOH SAM. "O_w" represents the oxygen atom in water molecules.

An example simulation setup is shown in Figure 1a. Two solid gold (111) substrates with face-centered cubic lattice were placed at both ends (50 layers on each side) of the simulation box. The SAMs are placed by generating an 8 × 8 array of single thiol chains with the initial tilt angle of 30° and a S−S spacing of 0.497 nm.[29] A total of 2000 water molecules are compacted into the space between the two substrates using Packmol.[45]

NEMD simulations are performed to calculate the ITC. The Langevin thermostats are used to thermostat the heat source at 310 K and the heat sink at 210 K so that one of the interfaces is near room temperature (~300 K). For the simulation procedure, the simulation system is first equilibrated in a canonical ensemble (*NVT*) at 260 K for 0.5 ns. The system is optimized in an isothermal−isobaric ensemble (*NPT*) at 1 atm and 260 K for another 1 ns. After the

DOI: 10.1021/acsami.8b03709
ACS Appl. Mater. Interfaces 2018, 10, 28159−28165

structures are fully equilibrated, to prevent the heat leakage during the heat-transfer process, we fixed the last three layers of gold atoms at each side and add extra vacuum space. Then the microcanonical ensemble (*NVE*) is then applied to the simulation, which lasts 3 ns, and the last 1 ns is chosen as the production period to calculate the ITC and the error bars are the standard deviations of the data from the period. Figure 1b shows a typical steady-state temperature profile. When the nonequilibrium state becomes steady, the ITC is calculated using $G = q/\Delta T$, where G is the ITC, q is the heat flux, and ΔT is the temperature gap at the higher temperature interface (~300 K) obtained by extrapolating the linear fits of temperature profiles of Au and water to the interface.

RESULTS AND DISCUSSION

The calculated ITC values are 51 ± 9, 155 ± 13, and 187 ± 9 MW/m^2 K for the −CH_3, −OH, and −COOH SAM-functionalized Au−water interfaces, respectively. Our results agree reasonably with time-domain thermoreflectance experiments,[22] which reported ITC values of 65 ± 5 and 190 ± 30 MW/m^2 K for a −CH_3 SAM- and a −OH SAM-functionalized Au−water interface, respectively. The slight differences between our simulation results and those from experiments may be attributed to the uncertainty in the experimental sample (e.g., defects) and the accuracy of the MD potentials. The interface energies of these three interfaces are, respectively, 68 266 and 340 kcal/mol. As expected, the polarized SAM interfaces (−OH and −COOH SAMs) have much larger interface energies than that of the nonpolar SAM interface (−CH_3 SAM), which agrees with experiments.[22,46] A couple of experimental measurements[46] show that the −OH SAM and the −COOH SAM have very similar water contact angles within the uncertainty of each other, but the −OH SAM is slightly more hydrophilic than the −COOH SAM. We note that these measurements only measured the advancing contact angle without considering the hysteresis effect. The real contact angle for the SAM surface should range between the advancing and the receding contact angles. Harikrishna et al.[22] indeed find that the receding contact angle of the −COOH SAM is smaller than that of the −OH SAM. In addition, factors such as the pH and surface roughness in Keselowsky's experiment[46] might also have impacted the measured contact angles. Nevertheless, our simulation results are self-consistent within the scope of this present study, and we believe that the intrinsic interfacial binding energy of the −COOH SAM interface should be larger than that of the −OH SAM interface because −COOH can provide two hydrogen binding sites.

As expected, we can see that the interface with the most polarized −COOH SAM has the highest value of ITC, whereas that with the nonpolar −CH_3 SAM has the lowest. We plot the ITCs of the three different systems as a function of the corresponding absolute values of the interfacial adhesion energy, calculated as the sum of all interactions between the water and the SAM-functionalized Au substrate, and found a linear relation in the data (Figure 2). Such an observation is consistent with the previous results from MD simulations and experiments.[21,22] Although this trend is known to be common, the microscopic origin of such observations has never been studied in detail.

At the molecular level, the thermal energy transport across the interface is realized by atoms at either side of the interface doing work to one another across the interface.[32,47] The rate of this work (i.e., power, p) exchanged between the SAM-functionalized substrate and water can be calculated as

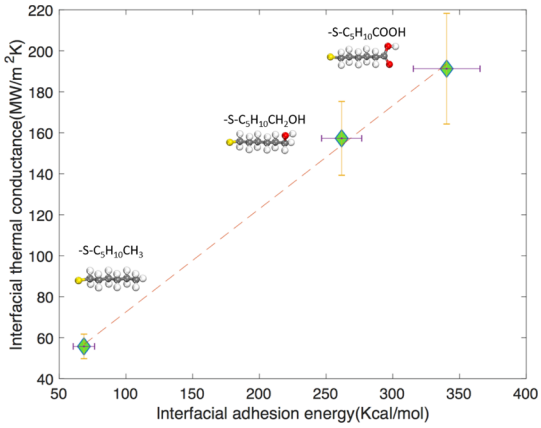

Figure 2. ITC as a function of the interfacial adhesion energy for water contacting differently functionalized Au surfaces. Stronger interfacial adhesion energy leads to larger ITC. The dashed line is a linear fit.

$$p = \frac{1}{2}\left\{\sum_{i\in \mathrm{sub}/j\in \mathrm{w}} F_{ij}\cdot v_j - \sum_{i\in \mathrm{sub}/j\in \mathrm{w}} F_{ji}\cdot v_i\right\} \quad (3)$$

where F_{ij} is the force from atom j exerted on atom i and v is the atom velocity. The indexes i and j belong to the SAM-functionalized substrate (sub) and water (w), respectively. We note that this equation for the interface heat flux can be shown equivalent to the equation by Torii et al.[48] who derived a similar equation for bulk heat flux from the Irving and Kirkwood relation.[49] This power normalized by the interface area leads to the heat flux $q = p/A$, where A is the cross-sectional area. As can been seen, the heat flux across the interface is related to the dynamics of the atoms (i.e., v) and interatomic forces. It is not directly related to the interfacial adhesion energy but instead its derivative (i.e., force, F). Furthermore, the total exchanged power can be separated using the following equation:

$$\begin{aligned} p &= p^{\mathrm{L\text{-}J}} + p^{\mathrm{Q}} \\ &= \frac{1}{2}\left\{\sum_{i\in \mathrm{sub}/j\in \mathrm{w}} F_{ij}^{\mathrm{L\text{-}J}}\cdot v_j - \sum_{i\in \mathrm{sub}/j\in \mathrm{w}} F_{ji}^{\mathrm{L\text{-}J}}\cdot v_i\right\} \\ &\quad + \frac{1}{2}\left\{\sum_{i\in \mathrm{sub}/j\in \mathrm{w}} F_{ij}^{\mathrm{Q}}\cdot v_j - \sum_{i\in \mathrm{sub}/j\in \mathrm{w}} F_{ji}^{\mathrm{Q}}\cdot v_i\right\} \end{aligned} \quad (4)$$

The ITC can thus also be decomposed into the L-J and the electrostatic portions according to $G^{\mathrm{L\text{-}J}} = q^{\mathrm{L\text{-}J}}/\Delta T$ or $G^{\mathrm{Q}} = q^{\mathrm{Q}}/\Delta T$. As shown in Figure 3a, when the surface functionalization changes from the nonpolar −CH_3 SAM to the polar −OH SAM, both the L-J and the electrostatic portions of the ITC increase dramatically. From the −OH SAM to the more polar −COOH SAM, the electrostatic portion of ITC does not show an obvious increase, but the L-J portion is enhanced significantly. Such a finding is slightly surprising, because it would be intuitive to postulate that it is the increased electrostatic interaction due to the more polar SAM groups that contribute mainly to the increase in ITC. However, our data show that as the SAM becomes polarized, the stronger electrostatic interaction will not only enhance the thermal energy transported by the electrostatic forces themselves but also enhance that by the L-J forces. In Figure 3b, the total

DOI: 10.1021/acsami.8b03709
ACS Appl. Mater. Interfaces 2018, 10, 28159−28165

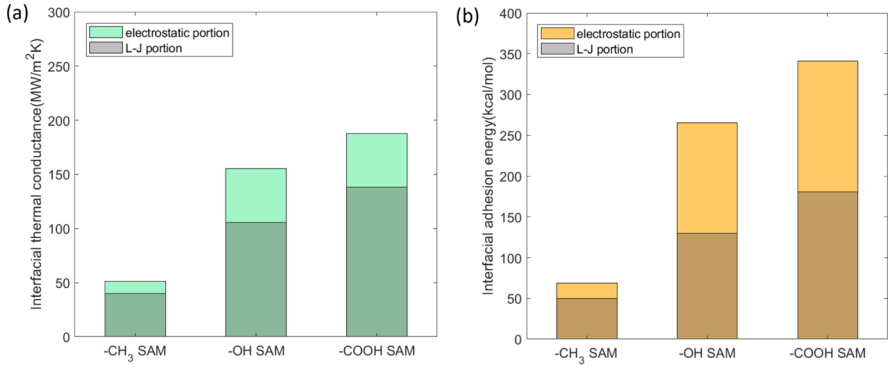

Figure 3. (a) Decomposition of ITC into contributions from the L-J interaction (the grayed portion) and electrostatic interactions (the bright portion). (b) Decomposition of interfacial adhesion energy into contributions from L-J interaction (the grayed portion) and electrostatic interactions (the bright portion).

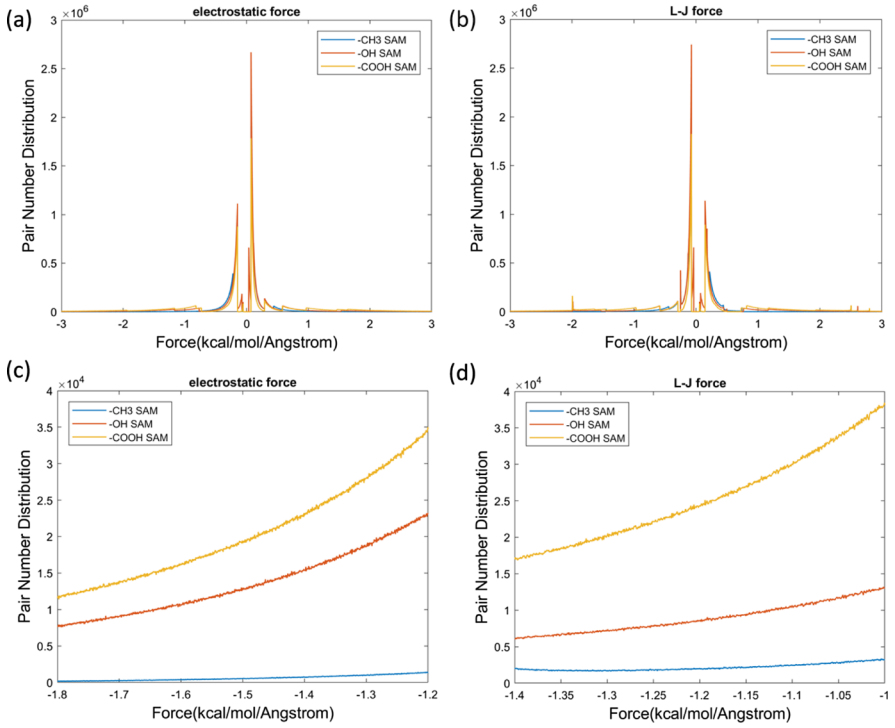

Figure 4. Force distribution of the (a) electrostatic and (b) L-J interactions between the substrate (Au + SAM) and water with a full *y*-axis view range. (c,d) are respective replots of panels (a,b) but with a zoomed view range.

interfacial adhesion energy is also decomposed into the L-J and electrostatic portions. Similar to the ITC decomposition, both L-J and electrostatic adhesion energy increase significantly from the $-CH_3$ to the $-OH$ SAM. From the $-OH$ to the $-COOH$ SAM, the increase in L-J energy is obvious, whereas the electrostatic portion only increases slightly. Such effects are consistent with the SAM-induced thermal transport enhancement across interfaces,[15,29] as seen in other simulations.

Because the atomic velocities are expected to be similar in all three cases because of the same temperature, according to eq 1, the interatomic forces are the only reason for the above observation in ITC (Figure 3a). To analyze the forces across the interfaces, the number distribution of the pairwise forces across the interface as a function of the force magnitude is shown in Figure 4 as a histogram, where electrostatic and L-J forces are plotted separately. The positive force indicates repulsion between two atoms, whereas the negative force means attraction. There is a large population around zero in both Figure 4a,b, which indicates weak forces between atoms that have long distances from each other. Panels c and d in Figure 4 display the same data as those in panels a and b but with different view ranges in the *x*-axis to enable a clearer comparison. From the nonpolar SAM ($-CH_3$) to the highly polar SAM ($-COOH$), the number of interacting atom pairs increases for both electrostatic and L-J interactions as shown in Figure 4c,d (i.e., higher number distribution of pairwise interactions from the blue line to the red line and then to the orange line). This trend is also confirmed in Table 2, where we calculate the total L-J and electrostatic force and the total number of pair interactions for each interface using $f_{total} = \sum N \cdot f$, where N is the number of interaction pairs and f is the force between the pair.

Table 2 also shows that for the $-CH_3$ SAM interface, the attractive forces (negative) are from the L-J interaction, whereas the electrostatic forces are mainly repulsive. On the contrary, for the $-OH$ and $-COOH$ SAM interfaces, the

DOI: 10.1021/acsami.8b03709
ACS Appl. Mater. Interfaces 2018, 10, 28159−28165

Table 2. Total L-J and Electrostatic Forces and Total Number of Pair Interactions within the Cutoff between the Substrate (Au + SAM) and Water for the Three Interfaces[a]

interface	total L-J	total electrostatic	total pair numbers
$-CH_3$	-8.3×10^4	2.6×10^4	3.7×10^8
$-OH$	8.9×10^5	-9.7×10^5	4.3×10^8
$-COOH$	1.3×10^6	-1.5×10^6	4.8×10^8

[a]The force unit is kcal mol^{-1} Å^{-1}.

attractive forces are from the electrostatic interaction, whereas the L-J forces are repulsive. Because the repulsive part in the L-J interaction can have a larger gradient than that of the attractive part, the overall repulsive forces can be larger than the attractive forces across the interface. Because the heat flux (eqs 3 and 4) is expressed as the force multiplied by the atomic velocity, the repulsive part in the L-J interaction can contribute more significantly to the ITC. We further calculate the summation of the magnitudes of the repulsive forces and that of the attractive forces across the interfaces and found their ratios to be 1.1, 1.9, and 2.1 for the $-CH_3$, $-OH$, and $-COOH$ SAM interfaces, respectively. The repulsive forces are indeed larger than the attractive forces in all cases, and this difference increases as the SAM molecules become more polarized.

In addition, Table 2 also shows that the more polar the interface ($-COOH$ > $-OH$ > $-CH_3$) is, the larger the number of interacting atom pairs. These observations suggest that the stronger electrostatic interaction due to the polar SAM groups attracts water molecules closer to the interface, which should have led to a higher water density at the interface, and thus, there are more water molecules interacting with the SAM molecules via both electrostatic and L-J interactions. This implication can be proven by characterizing the water structure in the vicinity of the interfaces. We first plot the water mass density along the z-direction as shown in Figure 5a. When the SAM changes from the nonpolar $-CH_3$ group to the highly polar $-COOH$ group, the water density profile moves closer to the SAM surface. This suggests that the stronger electrostatic interaction can attract water molecules closer to the interface, reducing the interaction distance and thus leading to larger effective forces from both the electrostatic interaction and the L-J interaction. Moreover, the amplitudes of the water density peaks near the interface also increase, which suggests that there are more atoms participating in the power exchange across the interface. Both factors will lead to more efficient power exchange across the interfaces, thus resulting in higher ITC. The local water distribution near the interface is also characterized by the radial distribution function (RDF, Figure 5b) calculated as $g(r) = n(r)/(4\pi r^2 \rho \Delta r)$, where $n(r)$ is the number of atoms in a shell of thickness Δr at a distance r from the reference atom and ρ is the average water atom number density. For the $-CH_3$ SAM, we take the C atom in the CH_3 end group as the reference atom, whereas for the $-OH$ and $-COOH$ SAMs, the reference atoms are chosen as the oxygen atom in the hydroxyl group. As expected, the RDF shows that from $-CH_3$ to $-OH$ and then to $-COOH$ SAM, the peaks shift from the right to the left, which directly indicate progressively shorter distances between the thiol end groups and water molecules.

CONCLUSIONS

In summary, we have calculated the ITC of Au−water interfaces with different SAM functionalizations. We find that when the SAM end group becomes more polar, the ITC becomes larger. Combining the heat flux decomposition to different interatomic interactions across interfaces and analyses of water structures close to the functionalized surfaces, we found that there is a collaborative effect from electrostatic and L-J interactions. The electrostatic interactions, which are between the polar functional groups of SAMs and water, will attract water molecules closer to the solid surface, leading both the electrostatic interaction and the L-J interaction (especially the repulsive part) to have larger effective forces across the interfaces. This increases the power exchanged between solid and water atoms, enhancing the thermal energy transport. The results from this work will provide new insights to the understanding of thermal transport across solid−water interfaces.

AUTHOR INFORMATION

Corresponding Author

*E-mail: tluo@nd.edu.

ORCID

Dezhao Huang: 0000-0002-1413-5438
Ruimin Ma: 0000-0003-1527-9289
Tengfei Luo: 0000-0003-3940-8786

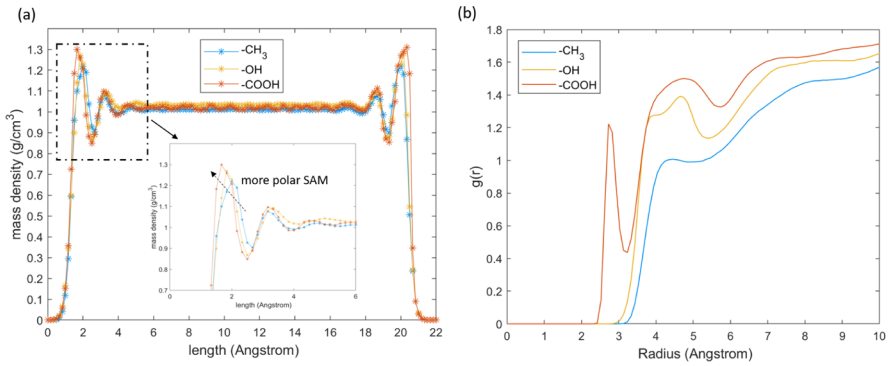

Figure 5. (a) Water density profiles near the $-CH_3$ SAM, $-OH$ SAM, and $-COOH$ SAM surfaces. (b) RDF of the oxygen atoms in water molecules with respect to the carbon atoms in the methyl group of the $-CH_3$ SAM and the oxygen atoms in the hydroxyl groups of the $-OH$ and $-COOH$ SAMs.

DOI: 10.1021/acsami.8b03709
ACS Appl. Mater. Interfaces 2018, 10, 28159−28165

Present Address

[§]Materials Science, Schrodinger, New York, NY 10035, United States

Notes

The authors declare no competing financial interest.

■ ACKNOWLEDGMENTS

D.H. acknowledges the financial support from the Chinese Scholarship Council. T.L. thanks the support from the NSF (1706039) and the Dorini Family for the endowed professorship in Energy Studies. T.L. also thanks the support from The Center for the Advancement of Science in Space (CASIS) (GA-2018-268). The simulations are supported by the Notre Dame Center for Research Computing and NSF through XSEDE computing resources provided by SDSC Comet and Comet and TACC Stampede under grant number TG-CTS100078.

■ REFERENCES

(1) Yang, J.; Pang, Y.; Huang, W.; Shaw, S. K.; Schiffbauer, J.; Pillers, M. A.; Mu, X.; Luo, S.; Zhang, T.; Huang, Y.; Li, G.; Ptasinska, S.; Lieberman, M.; Luo, T. Functionalized Graphene Enables Highly Efficient Solar Thermal Steam Generation. *ACS Nano* **2017**, *11*, 5510−5518.

(2) Trieb, F.; Müller-Steinhagen, H. Concentrating Solar Power for Seawater Desalination in the Middle East and North Africa. *Desalination* **2008**, *220*, 165−183.

(3) Koschikowski, J.; Wieghaus, M.; Rommel, M. Solar Thermal-Driven Desalination Plants Based on Membrane Distillation. *Desalination* **2003**, *156*, 295−304.

(4) Fath, H. E. S. Solar Distillation: A Promising Alternative for Water Provision with Free Energy, Simple Technology and a Clean Environment. *Desalination* **1998**, *116*, 45−56.

(5) Das, S. K.; Choi, S. U.; Yu, W.; Pradeep, T. Conduction Heat Transfer in Nano-fluids. *Nanofluids: Science and Technology*; Wiley, 2008.

(6) Eastman, J. A.; Phillpot, S. R.; Choi, S. U. S.; Keblinski, P. Thermal Transport in Nanofluids. *Annu. Rev. Mater. Res.* **2004**, *34*, 219−246.

(7) Mahian, O.; Kianifar, A.; Kalogirou, S. A.; Pop, I.; Wongwises, S. A Review of the Applications of Nanofluids in Solar Energy. *Int. J. Heat Mass Transfer* **2013**, *57*, 582−594.

(8) Qin, Z.; Bischof, J. C. Thermophysical and Biological Responses of Gold Nanoparticle Laser Heating. *Chem. Soc. Rev.* **2012**, *41*, 1191−1217.

(9) Zhang, T.; Luo, T. High-Contrast, Reversible Thermal Conductivity Regulation Utilizing the Phase Transition of Polyethylene Nanofibers. *ACS Nano* **2013**, *7*, 7592−7600.

(10) Chung, D. D. L. Thermal Interface Materials. *J. Mater. Eng. Perform.* **2001**, *10*, 56−59.

(11) West, J. L.; Halas, N. J. Engineered Nanomaterials for Biophotonics Applications: Improving Sensing, Imaging, and Therapeutics. *Annu. Rev. Biomed. Eng.* **2003**, *5*, 285−292.

(12) Huxtable, S. T.; Cahill, D. G.; Shenogin, S.; Xue, L.; Ozisik, R.; Barone, P.; Usrey, M.; Strano, M. S.; Siddons, G.; Shim, M.; Keblinski, P. Interfacial Heat Flow in Carbon Nanotube Suspensions. *Nat. Mater.* **2003**, *2*, 731−734.

(13) Barrat, J.; Chiaruttini, F. Kapitza resistance at the liquid-solid interface. *Mol. Phys.* **2003**, *101*, 1605−1610.

(14) Cahill, D. G.; Ford, W. K.; Goodson, K. E.; Mahan, G. D.; Majumdar, A.; Maris, H. J.; Merlin, R.; Phillpot, S. R. Nanoscale Thermal Transport. *J. Appl. Phys.* **2003**, *93*, 793−818.

(15) Cahill, D. G.; Braun, P. V.; Chen, G.; Clarke, D. R.; Fan, S.; Goodson, K. E.; Keblinski, P.; King, W. P.; Mahan, G. D.; Majumdar, A.; Maris, H. J.; Phillpot, S. R.; Pop, E.; Shi, L. Nanoscale thermal transport. II. 2003−2012. *Appl. Phys. Rev.* **2014**, *1*, 011305.

(16) Luo, T.; Chen, G. Nanoscale heat transfer—from computation to experiment. *Phys. Chem. Chem. Phys.* **2013**, *15*, 3389.

(17) Liao, Q.; Liu, Z.; Liu, W.; Deng, C.; Yang, N. Extremely High Thermal Conductivity of Aligned Carbon Nanotube-Polyethylene Composites. *Sci. Rep.* **2015**, *5*, 16543.

(18) Love, J. C.; Estroff, L. A.; Kriebel, J. K.; Nuzzo, R. G.; Whitesides, G. M. Self-Assembled Monolayers of Thiolates on Metals as a Form of Nanotechnology. *Chem. Rev.* **2005**, *105*, 1103−1170.

(19) Wei, X.; Zhang, T.; Luo, T. Thermal Energy Transport across Hard-Soft Interfaces. *ACS Energy Lett.* **2017**, *2*, 2283−2292.

(20) Ge, Z.; Cahill, D. G.; Braun, P. V. Thermal Conductance of Hydrophilic and Hydrophobic Interfaces. *Phys. Rev. Lett.* **2006**, *96*, 186101.

(21) Shenogina, N.; Godawat, R.; Keblinski, P.; Garde, S. How Wetting and Adhesion Affect Thermal Conductance of a Range of Hydrophobic to Hydrophilic Aqueous Interfaces. *Phys. Rev. Lett.* **2009**, *102*, 156101.

(22) Harikrishna, H.; Ducker, W. A.; Huxtable, S. T. The influence of interface bonding on thermal transport through solid-liquid interfaces. *Appl. Phys. Lett.* **2013**, *102*, 251606.

(23) Tian, Z.; Marconnet, A.; Chen, G. Enhancing Solid-Liquid Interface Thermal Transport Using Self-Assembled Monolayers. *Appl. Phys. Lett.* **2015**, *106*, 211602.

(24) Luo, T.; Lloyd, J. R. Enhancement of Thermal Energy Transport Across Graphene/Graphite and Polymer Interfaces: A Molecular Dynamics Study. *Adv. Funct. Mater.* **2012**, *22*, 2495−2502.

(25) Wang, Y.; Yang, C.; Pei, Q.-X.; Zhang, Y. Some Aspects of Thermal Transport Across the Interface between Graphene and Epoxy in Nanocomposites. *ACS Appl. Mater. Interfaces* **2016**, *8*, 8272−8279.

(26) Wei, X.; Zhang, T.; Luo, T. Molecular Fin Effect from Heterogeneous Self-Assembled Monolayer Enhances Thermal Conductance across Hard-Soft Interfaces. *ACS Appl. Mater. Interfaces* **2017**, *9*, 33740−33748.

(27) Konatham, D.; Striolo, A. Thermal Boundary Resistance at the Graphene-Oil Interface. *Appl. Phys. Lett.* **2009**, *95*, 163105.

(28) Wang, Y.; Yang, C.; Pei, Q.-X.; Zhang, Y. Some Aspects of Thermal Transport across the Interface between Graphene and Epoxy in Nanocomposites. *ACS Appl. Mater. Interfaces* **2016**, *8*, 8272−8279.

(29) Hung, S.-W.; Kikugawa, G.; Shiomi, J. Mechanism of Temperature Dependent Thermal Transport across the Interface between Self-Assembled Monolayer and Water. *J. Phys. Chem. C* **2016**, *120*, 26678−26685.

(30) Acharya, H.; Mozdzierz, N. J.; Keblinski, P.; Garde, S. How Chemistry, Nanoscale Roughness, and the Direction of Heat Flow Affect Thermal Conductance of Solid-Water Interfaces. *Ind. Eng. Chem. Res.* **2012**, *51*, 1767−1773.

(31) Kikugawa, G.; Ohara, T.; Kawaguchi, T.; Kinefuchi, I.; Matsumoto, Y. A Molecular Dynamics Study on Heat Conduction Characteristics Inside the Alkanethiolate SAM and Alkane Liquid. *Int. J. Heat Mass Transfer* **2014**, *78*, 630−635.

(32) Domingues, G.; Volz, S.; Joulain, K.; Greffet, J.-J. Heat Transfer between Two Nanoparticles Through Near Field Interaction. *Phys. Rev. Lett.* **2005**, *94*, 085901.

(33) Sun, F.; Zhang, T.; Jobbins, M. M.; Guo, Z.; Zhang, X.; Zheng, Z.; Tang, D.; Ptasinska, S.; Luo, T. Molecular Bridge Enables Anomalous Enhancement in Thermal Transport across Hard-Soft Material Interfaces. *Adv. Mater.* **2014**, *26*, 6093−6099.

(34) Luo, T.; Lloyd, J. R. Equilibrium Molecular Dynamics Study of Lattice Thermal Conductivity/Conductance of Au-SAM-Au Junctions. *J. Heat Transfer* **2010**, *132*, 032401.

(35) Luo, T.; Lloyd, J. R. Non-equilibrium molecular dynamics study of thermal energy transport in Au-SAM-Au junctions. *Int. J. Heat Mass Transfer* **2010**, *53*, 1−11.

(36) Jaeger, R.; Lagowski, J. B.; Manners, I.; Vancso, G. J. Ab Initio Studies on the Structure, Conformation, and Chain Flexibility of Halogenated Poly(Thionylphosphazenes). *Macromolecules* **1995**, *28*, 539−546.

DOI: 10.1021/acsami.8b03709
ACS Appl. Mater. Interfaces 2018, 10, 28159−28165

(37) Mark, P.; Nilsson, L. Structure and Dynamics of the TIP3P, SPC, and SPC/E Water Models at 298 K. *J. Phys. Chem. A* **2001**, *105*, 9954−9960.
(38) MacKerell, A. D.; Bashford, D.; Bellott, M.; Dunbrack, R. L.; Evanseck, J. D.; Field, M. J.; Fischer, S.; Gao, J.; Guo, H.; Ha, S.; Joseph-McCarthy, D.; Kuchnir, L.; Kuczera, K.; Lau, F. T. K.; Mattos, C.; Michnick, S.; Ngo, T.; Nguyen, D. T.; Prodhom, B.; Reiher, W. E.; Roux, B.; Schlenkrich, M.; Smith, J. C.; Stote, R.; Straub, J.; Watanabe, M.; Wiórkiewicz-Kuczera, J.; Yin, D.; Karplus, M. All-Atom Empirical Potential for Molecular Modeling and Dynamics Studies of Proteins. *J. Phys. Chem. B* **1998**, *102*, 3586−3616.
(39) Sun, H. COMPASS: An ab Initio Force-Field Optimized for Condensed-Phase ApplicationsOverview with Details on Alkane and Benzene Compounds. *J. Phys. Chem. B* **1998**, *102*, 7338−7364.
(40) Zhang, T.; Gans-Forrest, A. R.; Lee, E.; Zhang, X.; Qu, C.; Pang, Y.; Sun, F.; Luo, T. Role of Hydrogen Bonds in Thermal Transport across Hard/Soft Material Interfaces. *ACS Appl. Mater. Interfaces* **2016**, *8*, 33326−33334.
(41) Rappe, A. K.; Casewit, C. J.; Colwell, K. S.; Goddard, W. A.; Skiff, W. M. UFF, a Full Periodic Table Force Field for Molecular Mechanics and Molecular Dynamics Simulations. *J. Am. Chem. Soc.* **1992**, *114*, 10024−10035.
(42) Zhang, T.; Gans-Forrest, A. R.; Lee, E.; Zhang, X.; Qu, C.; Pang, Y.; Sun, F.; Luo, T. Role of Hydrogen Bonds in Thermal Transport across Hard/Soft Material Interfaces. *ACS Appl. Mater. Interfaces* **2016**, *8*, 33326−33334.
(43) Plimpton, S. Fast Parallel Algorithms for Short-Range Molecular Dynamics. *J. Comput. Phys.* **1995**, *117*, 1−19.
(44) Zhang, T.; Luo, T. Role of Chain Morphology and Stiffness in Thermal Conductivity of Amorphous Polymers. *J. Phys. Chem. B* **2016**, *120*, 803−812.
(45) Martínez, L.; Andrade, R.; Birgin, E. G.; Martínez, J. M. PACKMOL: A Package for Building Initial Configurations for Molecular Dynamics Simulations. *J. Comput. Chem.* **2009**, *30*, 2157−2164.
(46) Keselowsky, B. G.; Collard, D. M.; García, A. J. Surface chemistry modulates fibronectin conformation and directs integrin binding and specificity to control cell adhesion. *J. Biomed. Mater. Res., Part A* **2003**, *66*, 247−259.
(47) Chalopin, Y.; Esfarjani, K.; Henry, A.; Volz, S.; Chen, G. Thermal Interface Conductance in Si/Ge Superlattices by Equilibrium Molecular Dynamics. *Phys. Rev. B: Condens. Matter Mater. Phys.* **2012**, *85*, 195302.
(48) Torii, D.; Nakano, T.; Ohara, T. Contribution of Inter- and Intramolecular Energy Transfers to Heat Conduction in Liquids. *J. Chem. Phys.* **2008**, *128*, 044504.
(49) Irving, J. H.; Kirkwood, J. G. The Statistical Mechanical Theory of Transport Processes. IV. The Equations of Hydrodynamics. *J. Chem. Phys.* **1950**, *18*, 817−829.

DOI: 10.1021/acsami.8b03709
ACS Appl. Mater. Interfaces 2018, 10, 28159−28165